

LETTER TO THE EDITOR

# GLIMPSE-D: Metallicity Decline in Faint Galaxies: Implications for [O III]+H $\beta$ Luminosity Function and Reionisation Budget

Damien Korber<sup>1\*</sup>, Daniel Schaefer<sup>1,2</sup>, Rui Marques-Chaves<sup>1</sup>, Angela Adamo<sup>14</sup>, Arghyadeep Basu<sup>5</sup>, John Chisholm<sup>9,10</sup>, Miroslava Dessauges-Zavadsky<sup>1</sup>, Kristen. B. W. McQuinn<sup>3,4</sup>, Alberto Saldana-Lopez<sup>6</sup>, Hakim Atek<sup>11</sup>, Ryan Endsley<sup>9</sup>, Seiji Fujimoto<sup>7,8</sup>, Lukas J. Furtak<sup>9,10</sup>, Vasily Kokorev<sup>9</sup>, Rohan P. Naidu<sup>13</sup>, and Richard Pan<sup>12</sup>

(Affiliations can be found after the references)

Received MONTH DAY, YEAR; accepted MONTH DAY, YEAR

## ABSTRACT

We report the measurement of the  $R3=[\text{O III}]\lambda 5008/\text{H}\beta$  ratios for 54 galaxies in the GLIMPSE-D survey. Thanks to gravitational lensing, our sample includes galaxies with  $-20 \lesssim M_{\text{UV}} < -14$  at  $z = 6 - 9$ . We derive oxygen abundances using calibrated relationships. We observe a significant decline in  $R3$  values below  $M_{\text{UV}} \gtrsim -18$ , which we interpret as evidence of decreasing metallicities in fainter regimes. We explore four prescription models of the evolution of  $R3$  with UV emission based on the new measurements and results from previous surveys. Applying these models to the GLIMPSE [O III]+H $\beta$  luminosity functions, we measure and extrapolate the ionising photon production rate  $\dot{N}_{\text{ion}}$  of galaxies down to very faint limits ( $\text{SFR}_{\text{H}\alpha} \gtrsim 5 \times 10^{-3} M_{\odot} \text{yr}^{-1}$ ). Our results support the dominant contribution of star-forming galaxies to reionisation, and are consistent with the recent discovery of ultra-faint metal-poor galaxies. Our measurements of the relative contribution of each luminosity bin show that galaxies with  $L_{\text{H}\alpha} \approx 10^{41-42} \text{erg s}^{-1}$  dominate at  $8 < z < 9$ , but the relative contributions become more uniform at  $7 < z < 8$ . Extreme models either under- or over-estimate the ionising photon budget, while intermediate models align with recent observational constraints.

**Key words.** some keywords – separated by two dash lines

## 1. Introduction

During the epoch of reionisation, the Universe underwent significant evolution which shaped its current aspect. This epoch ended around  $z \sim 5 - 6$  (e.g. Robertson 2022) with a fully ionised Universe. While main drivers of reionisation are well accepted, their relative importance remains uncertain. Some scenarios emphasise the dominant role of faint galaxies (e.g. Atek et al. 2018; Simmonds et al. 2024), other highlight brighter galaxies (e.g. Naidu et al. 2020), while others attribute a significant contribution to AGNs (e.g. Singha et al. 2025; Grazian et al. 2024). Constraining the number density of galaxies and ionizing photon production is essential for understanding their role in cosmic reionisation. While previous works have mostly used the UV luminosity functions (LF) at different redshifts (e.g. Bouwens et al. 2022), the relation between the UV luminosity and ionizing photon emission is complex. On the other hand, the LF of emission lines, provides a more direct measure of the ionizing photon production, which can be achieved in the epoch of reionisation, e.g. with the [O III]+H $\beta$  LF at  $z \sim 6 - 9$ .

Using the ultra-deep GLIMPSE photometry (Atek et al. 2025), Korber et al. (2025) determined the very faint-end of the [O III]+H $\beta$  LF, finding an LF flatter than the UV LF, i.e. effectively a reduced number density of [O III]+H $\beta$  faint galaxies and a lower ionizing photon production than inferred with standard assumptions from the UV LF. To do so, they had to assume a dependence of  $R3=[\text{O III}]\lambda 5008/\text{H}\beta$  on  $M_{\text{UV}}$  to separate [O III] $\lambda 5008$  and H $\beta$ . These hypotheses were based on previous works probing mostly brighter galaxies, and extrapolations from lower redshift. Here we report a new statistical sample of [O III] $\lambda 5008$  and H $\beta$  measurements for galaxies observed with

deep medium G395M NIRSpec/JWST spectroscopy behind the strong lensing cluster Abell S1063, which robustly constrains the dependence of  $R3$  and metallicity on  $M_{\text{UV}}$  down to very faint objects at  $z \sim 6 - 7$ . This allows us to better quantify the impact of the faintest galaxies on cosmic reionisation.

## 2. Observations and data

The GLIMPSE-D program (DD-9223: Fujimoto et al. 2025) observed the strong lensing cluster Abell S1063 with the JWST/NIRSpec MSA instrument using the G395M grating, to obtain rest-optical emission line spectra of some of the intrinsically faintest galaxies at  $z \gtrsim 6$  (GLIMPSE, Atek et al. 2025). Most of the galaxies were observed for  $\sim 9 - 11$  h, but a subset was observed multiple times, with total integration times up to  $\sim 30$  h. The reduction followed Fujimoto et al. (2025) and resulted in 61 galaxies with robust redshifts at  $6 < z < 9$ . For objects with multiple spectra, we stacked the data by averaging the flux in each wavelength bin and propagating the associated uncertainties. We visually examined the 1D and 2D spectra, identifying spectra with missing information at the location of [O III] and H $\beta$ . Seven galaxies were discarded, leaving a final robust sample of 54 galaxies. The line flux of [O III] and H $\beta$  were measured using three Gaussian profiles, fitted with a standard Monte-Carlo Markov-Chain procedure, as detailed in App. A.  $M_{\text{UV}}$  was derived from the GLIMPSE photometric (Kokorev et al. 2025) catalogue and our spectroscopic redshifts. All the measured properties are tabulated in Table C.1.

To expand the parameter space probed in  $R3$  and  $M_{\text{UV}}$  we also used public data, taken from two main surveys: the very deep and large but unlensed field JADES DR4 (Scholtz et al. 2025) and the deep, lensed, but small volume survey UN-

\* Corresponding author: damien.korber@protonmail.ch

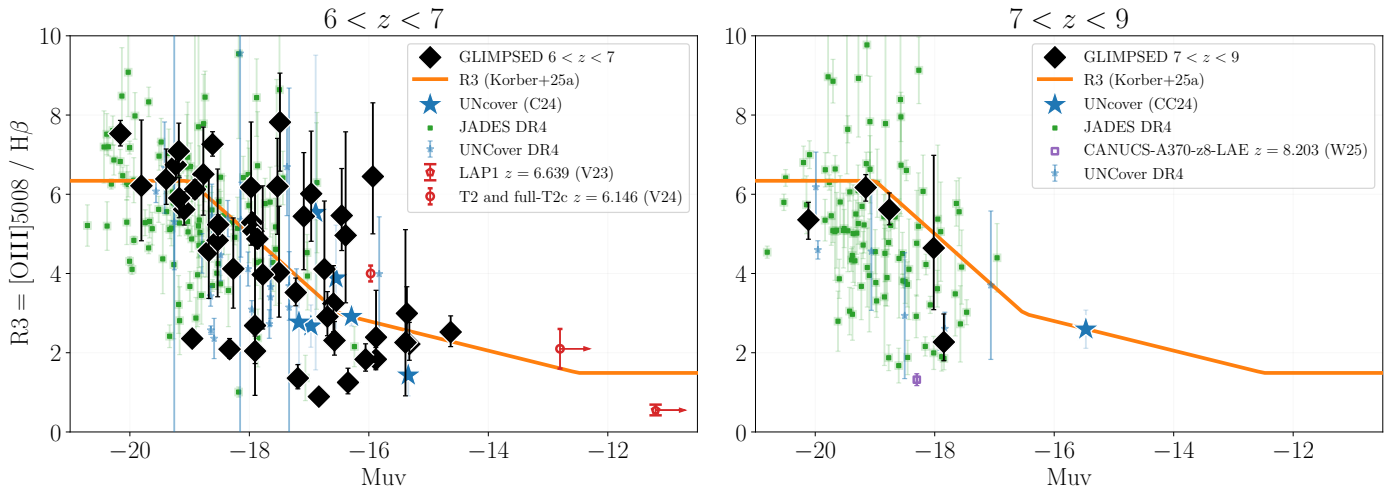


Fig. 1: Evolution of the R3 ratio as function of  $M_{\text{UV}}$  for the GLIMPSE-D galaxies, as well as the public JADES DR4 (Scholtz et al. 2025) and UNCOVER DR4 (Price et al. 2025) and (C24: Chemerynska et al. 2024). We further included the few very metal poor galaxies detected between redshift  $6 < z < 9$  (V23,V24: Vanzella et al. (2023, 2024); W25: Willott et al. (2025)). We also show the evolution as assumed in Korber et al. (2025). **Left:**  $6 < z < 7$  redshift range that includes many new objects from GLIMPSE-D in the very faint end. **Right:**  $7 < z < 9$  redshift range corresponding to the ranges with  $[\text{O III}]+\text{H}\beta$  in the F444W NIRCam filter, as discussed in Korber et al. (2025).

Cover (Bezanson et al. 2024; Suess et al. 2024; Furtak et al. 2023; Price et al. 2025). Since some of the sources in JADES were observed in multiple gratings, we measured their average flux and propagated the uncertainties. For UNCover we used the values of Chemerynska et al. (2024) for the faintest galaxies and we filtered out four clear Little Red Dots around  $R3 \sim 0.1$ .

### 3. Results and discussions

#### 3.1. $[\text{O III}]\lambda 5008$ emission and metallicity estimates of the faintest galaxies

Figure 1 presents our R3 measurements as a function of  $M_{\text{UV}}$  for two redshift bins. While intended to explore potential evolution across redshift, the sample lacks observations of faint ( $M_{\text{UV}} \geq -17$ ) galaxies at  $z > 7$ . Given this limitation, we assume no evolution over  $z = 6 - 9$  in the following analysis. All further  $R3(M_{\text{UV}})$  relationships will be based on the full  $z = 6 - 9$  dataset. GLIMPSE-D significantly expands the sample of galaxies with R3 measurements at magnitude fainter than  $M_{\text{UV}} \gtrsim -16$  at  $6 < z < 7$ . Our measurements show a decline of R3 in fainter galaxies. The decline in R3 is significant (Bootstrapped spearman with  $N=1000$ :  $\text{stat} = -0.42 \pm 0.03$ ,  $\text{pval} < 0.05$ ). This behaviour matches the proposed relationship from Korber et al. (2025), which was based on sparse data. At  $z \sim 7 - 9$ , the current data is poorly sampled below  $-18$ , but seem to show a hint of a decline as  $z \sim 6 - 7$  down to  $M_{\text{UV}} < -17$ . In the fainter regime, however, the limited sample of galaxies forces us to use the same dependence as for  $z = 6 - 7$ .

The  $[\text{O III}]\lambda 5008$ -to- $\text{H}\beta$  ratio is a commonly used indirect tracer of metallicity in star-forming galaxies (e.g. Sanders et al. 2025). Indeed, for metallicities  $12 + \log(\text{O/H}) \lesssim 8.0$ , R3 decreases monotonically towards low O/H, as also confirmed by photoionization models, for a given ionisation parameter (see e.g. Nakajima et al. 2024). Qualitatively, the observed decrease of R3 with  $M_{\text{UV}}$  is therefore expected from known mass-metallicity relationships, if  $M_{\text{UV}}$  also traces stellar mass to first order. To translate R3 to metallicity, we used the calibrated

$12 + \log(\text{O/H})$  measurements from Nakajima et al. (2022) (all samples calibration), assuming that the GLIMPSE-D objects are on the low-metallicity branch of the R3-O/H relation (i.e. at  $12 + \log(\text{O/H}) \lesssim 8.0$ ). Fig. 2 shows the resulting metallicities as a function of  $M_{\text{UV}}$ , spanning oxygen abundances of  $12 + \log(\text{O/H}) \sim 6.9 - 7.9$  ( $\sim 2 - 20$  % solar, adopting  $12 + \log(\text{O/H})_{\text{solar}} = 8.69$  from Asplund et al. (2009)). Objects around  $12 + \log(\text{O/H}) \sim 7.9$  have  $R3 \gtrsim 6$ , at or above the maximum of the R3 metallicity calibration from Nakajima et al. (2022). The lowest abundances are close to the observed metallicity floor at  $12 + \log(\text{O/H}) \sim 7.0$  found so far, both in low- $z$  and high- $z$  observations (e.g., Sanders et al. 2025; Nakajima et al. 2022). The UV-faint galaxies with extremely low metallicities remain challenging to observe due to their faint nebular features, as shown by recent observations at  $z \sim 6$  and other searches for extremely metal-poor galaxies (e.g. Morishita et al. 2025; Vanzella et al. 2025, 2024, 2023; Breneman et al. 2025). An in-depth analysis of the properties of the faintest ( $M_{\text{UV}} > -17$ ) GLIMPSE-D galaxies will be presented in Asada et al. (in prep).

#### 3.2. Impact of the faintest galaxies on reionisation

To describe the dependence of the R3 ratio on  $M_{\text{UV}}$  we propose four simple prescription models, based on the data available at  $6 < z < 9$ . Since the sample is at  $7 < z < 9$  is small, we assume that  $R3(M_{\text{UV}})$  does not evolve over  $6 < z < 9$ . *i*) A median value  $R3 = 5.1^{+1.6}_{-2.2}$ , independent of  $M_{\text{UV}}$ . It exhibits a fairly unrealistic view, as the MZR predicts a decrease of the oxygen abundance for fainter galaxies (e.g. Chemerynska et al. 2024), also supported by observations (e.g., Vanzella et al. 2023), but it provides a test of a homogeneous population in oxygen abundance. *ii*) A sigmoid fit of the running median. This model follows the observational data, with the assumption of a relatively high faint-end metallicity floor ( $\sim 4$  % solar) due to incompleteness at  $M_{\text{UV}} \gtrsim -16$ . *iii*) the same as *ii*) with a sharp cut-off at  $M_{\text{UV}} > -14$ , representing an extreme scenario where the very faint galaxy population is dominated by metal-poor galaxies. *iv*) the same as *ii*), with a faint-end metallicity floor fixed to the 16-

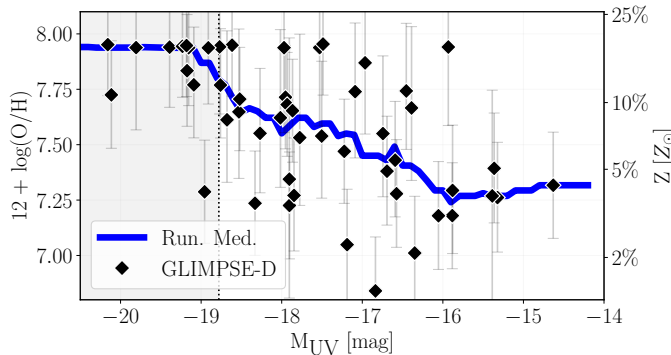


Fig. 2: Oxygen abundance of the selected GLIMPSE-D galaxies using the R3 calibration of Nakajima et al. (2022). Measurements and uncertainties for individual sources from R3 and the calibration are shown in black, and the oxygen abundance of the R3 running median is shown in blue.

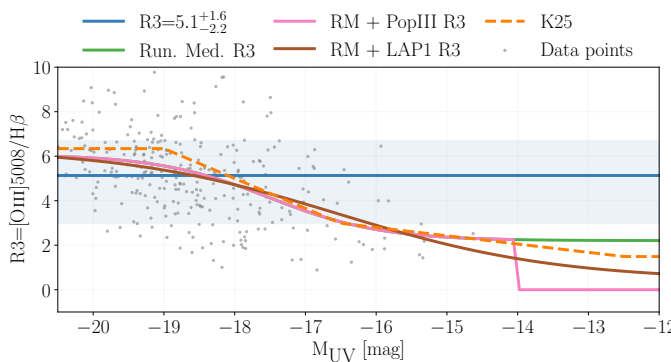


Fig. 3: Prescription models of R3(M<sub>UV</sub>) with the UNCOVER, JADES and GLIMPSE-D datapoints in the background.

84 percentile value of the most-metal poor object observed so far at our redshifts (LAP1 Vanzella et al. 2023). These scenarios are displayed in Fig. 3.

Using these models, we can now quantify the contribution of galaxies to cosmic reionisation following the procedure from Korber et al. (2025). In short, we determine the ionising photon production rate  $\dot{N}_{\text{ion}}$  from their [O III]+H $\beta$  LF, using our prescription models for R3( $M_{\text{UV}}$ ) to determine the contribution of H $\beta$ , and hence the H $\beta$  LF. Since hydrogen recombination lines are direct probes of the photoionisation rate, the integral over the H $\beta$  LF is a direct counter of the total ionising photon production rate, when a constant escape fraction of ionising photons,  $f_{\text{esc}}$ , is assumed. From this, the rate of photons available to reionise the IGM can be determined. See App. B for more details.

In Fig. 4 we show the cumulative ionising photon rate  $\dot{N}_{\text{ion}}$  from the two LFs of Korber et al. (2025) ( $7 < z < 8$  and  $8 < z < 9$ ), using the four prescription models for R3( $M_{\text{UV}}$ ) and assuming a constant  $f_{\text{esc}} = 14\%$  (Jecmen et al., submitted). In addition, we show the ionising photon production rate required to explain the observed ionisation state of the IGM at the considered redshifts, as inferred from Planck and multiple Ly $\alpha$  tracers (Mason et al. 2019; Bouwens et al. 2015).

We first focus on  $7 < z < 8$ . Due to the constant ionising contribution with model *i*), the  $\dot{N}_{\text{ion}}$  curve follows the LF and rapidly flattens, effectively undershooting the required budget. *ii)* provides a higher contribution of the faintest emitters and reaches the median budget of Mason et al. (2019). Model *iii)* strongly

differs from the others, predicting a very steep increase of  $\dot{N}_{\text{ion}}$ , effectively overshooting the budget, due to the postulated absence of [O III] emission in galaxies fainter than  $M_{\text{UV}} > -14$ . Such a scenario requires a drastic decrease of  $f_{\text{esc}}$  or a sharp decrease of the faint galaxies number density to lower the  $\dot{N}_{\text{ion}}$  budget.

For an integration limit of  $L_{\text{H}\alpha} \sim 10^{36} \text{ erg s}^{-1}$ , which corresponds to an SFR(H $\alpha$ )  $\sim 10^{-5} M_{\odot} \text{ yr}^{-1}$ , *i)* undershoots the median budget estimation of Mason et al. (2019) by  $\sim 0.25$  dex, meaning that a full contribution from galaxies require a factor  $\sim 1.8$  more ionising photon production rate. The budget can be reached by involving higher  $f_{\text{esc}}$ , but could also indicate contributions of AGNs. Models *ii)* and *iv)*, with an evolving R3, naturally predict more ionizing photons from faint galaxies. Finally, model *iv)*, which uses LAP1 (Vanzella et al. 2023) to constrain R3 of the faintest objects, slightly overshoots the photon budget of Bouwens et al. (2015) but is well within the estimations of Mason et al. (2019). These results provide evidence for model *iv)*, supporting a scenario where galaxies are the dominant drivers of reionisation, with only a minor role for alternative ionising sources. While the current number of detection of objects similar to LAP1 are very limited, this could simply be explained by observational biases, as such galaxies require peculiar conditions to be detected. In that scenario, the metallicity floor observed at  $12 + \log(\text{O/H}) \sim 7.0$  would be lower than currently observed (e.g. Sanders et al. 2025; Nakajima et al. 2022).

At redshift  $8 < z < 9$ , the very flat faint-end slope of the luminosity function results in all scenarios converging to the same outcome. Each model reaches the median ionising photon budget from Mason et al. (2019), indicating that galaxies are the primary drivers of reionisation in this redshift range. However, these estimations undershoot the older estimations from Bouwens et al. (2015). Notably, the relative contribution of each luminosity bin indicate that, in these scenarios, the reionisation is dominated by galaxies with  $L(\text{H}\alpha) \sim 10^{41-42} \text{ erg s}^{-1}$  and that faint emitters (i.e.  $< 10^{40} \text{ erg s}^{-1}$ ) contribute only negligibly to reionisation.

## 4. Conclusions

Using deep JWST NIRSpec observations of strongly lensed galaxies behind Abell S1063, we measured for the first time the R3=[O III]λ5008/H $\beta$  ratio of 54 very faint ( $\sim -20 \lesssim M_{\text{UV}} < -14$ ) galaxies. We found a significant turnover of R3 at  $M_{\text{UV}} \sim -18$  and a systematic decrease towards fainter UV magnitudes. We interpret the observed decrease as a decrease of the median O/H abundance (metallicity) for fainter galaxies, in agreement with expectations of lower metal enrichment in fainter and less massive galaxies (e.g. Sanders et al. 2025). We found metallicities down to  $\sim 2\%$  solar at  $M_{\text{UV}} \sim -17$ , close to the lowest metallicities observed in galaxies.

Using the observational data, we built four prescription models of the evolution of R3 with  $M_{\text{UV}}$ , and infer the contribution of galaxies to the ionising photon production budget from the recent measurements of the [O III]+H $\beta$  LF of Korber et al. (2025). We observed an undershooting and overshooting of the ionising photon budget predicted by Mason et al. (2019) for the extreme constant median R3 (*i*) and running median with faint-end Pop III cut (*iii*) models. Interestingly, intermediate models such as the running median sigmoid (*ii*) as well as the lower floor running median sigmoid (*iv*) both reach the budget from Mason et al. (2019), lowering earlier ionising photon production estimations (Muñoz et al. 2024). Finally, our results are consistent with a reionisation driven by star-forming galaxies, and ar-

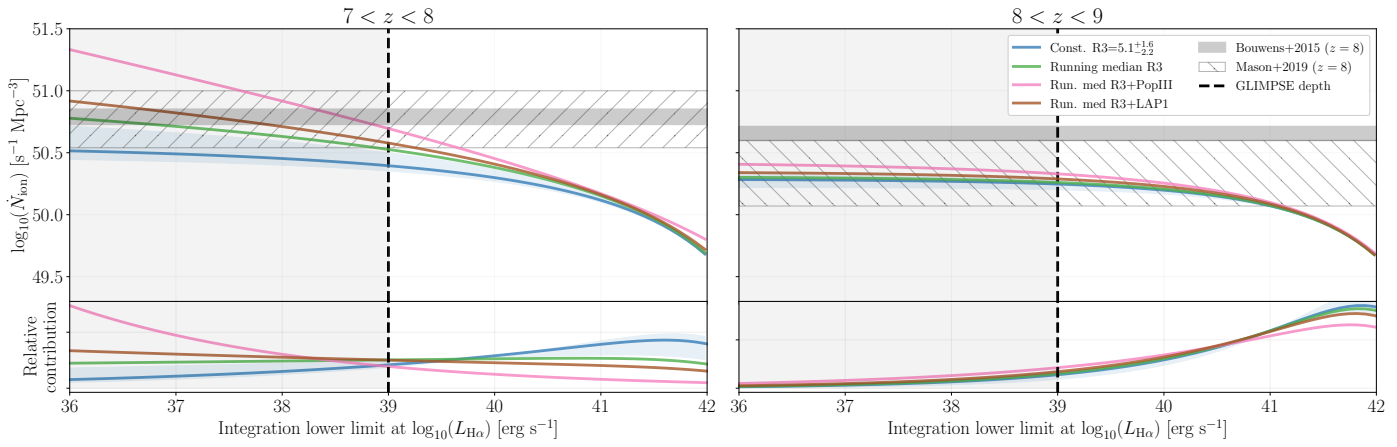


Fig. 4: Integrated ionising photon production rate  $\dot{N}_{\text{ion}}$  down to given  $L_{\text{H}\alpha}$ , measured from the GLIMPSE [O III]+H $\beta$  LF with the four R3 models (top panels), and the relative contribution of each luminosity bin to the ionising photon production rate (bottom panels). We use the average escape fraction measured for GLIMPSE  $f_{\text{esc}} = 14\%$  (Jecmen et al. Submitted). The left and right panels differentiate the LF from the two redshift bins from Korber et al. (2025). More details in App. B.

gue in favour of the existence of faint and metal-poor galaxies such as LAP1 (Vanzella et al. 2023). We show that the hypotheses on the decline of the average R3 with fainter  $M_{\text{UV}}$  from Korber et al. (2025) hold and are compatible with a lower metallicity floor, as shown by model iv). These results suggest that the faintest galaxies detected by GLIMPSE do not contribute significantly to the ionising budget during reionisation.

**Acknowledgements.** DK thanks Romain Meyer for the useful discussions on the project. AA acknowledges support by the Swedish research council Vetenskapsrådet (VR) project 2021-05559, and VR consolidator grant 2024-02061. This work is based [in part] on observations made with the NASA/ESA/CSA James Webb Space Telescope. The data were obtained from the Mikulski Archive for Space Telescopes at the Space Telescope Science Institute, which is operated by the Association of Universities for Research in Astronomy, Inc., under NASA contract NAS 5-03127 for JWST. These observations are associated with programs #9223 and #3293. **Softwares:** Emcee (Foreman-Mackey et al. 2013), Astropy (Collaboration et al. 2022), Numpy (Harris et al. 2020), Scipy (Virtanen et al. 2020), Matplotlib (Hunter 2007).

## References

Asplund, M., Grevesse, N., Sauval, A. J., & Scott, P. 2009, ARA&A, 47, 481  
 Atek, H., Chisholm, J., Kokorev, V., et al. 2025, arXiv e-prints, arXiv:2511.07542  
 Atek, H., Richard, J., Kneib, J.-P., & Schaefer, D. 2018, MNRAS, 479, 5184  
 Berg, D. A., Naidu, R. P., Chisholm, J., et al. 2025, eprint arXiv:2511.13591, arXiv:2511.13591  
 Bezanson, R., Labbe, I., Whitaker, K. E., et al. 2024, ApJ, 974, 92  
 Bouwens, R. J., Illingworth, G., Ellis, R. S., Oesch, P., & Stefanon, M. 2022, ApJ, 940, 55  
 Bouwens, R. J., Illingworth, G. D., Oesch, P. A., et al. 2015, ApJ, 811, 140  
 Breneman, J. A., McQuinn, K. B. W., Menchaca, A., et al. 2025, ApJ, 991, 191  
 Chemerynska, I., Atek, H., Dayal, P., et al. 2024, ApJ, 976, L15  
 Collaboration, A., Price-Whelan, A. M., Lim, P. L., et al. 2022, ApJ, 935, 167  
 Foreman-Mackey, D., Hogg, D. W., Lang, D., & Goodman, J. 2013, PASP, 125, 306  
 Fujimoto, S., Asada, Y., Naidu, R. P., et al. 2025, arXiv e-prints, arXiv:2512.11790  
 Furtak, L. J., Zitrin, A., Weaver, J. R., et al. 2023, MNRAS, 523, 4568  
 Grazian, A., Giallongo, E., Boutsia, K., et al. 2024, ApJ, 974, 84  
 Harris, C. R., Millman, K. J., van der Walt, S. J., et al. 2020, Nature, 585, 357  
 Hunter, J. D. 2007, Computing in Science & Engineering, 9, 90  
 Kokorev, V., Atek, H., Chisholm, J., et al. 2025, ApJ, 983, L22  
 Korber, D., Chemerynska, I., Furtak, L. J., et al. 2025, arXiv e-prints, arXiv:2510.04771  
 Mason, C. A., Naidu, R. P., Tacchella, S., & Leja, J. 2019, MNRAS, 489, 2669  
 Morishita, T., Liu, Z., Stiavelli, M., et al. 2025, arXiv e-prints, arXiv:2507.10521  
 Muñoz, J. B., Mirocha, J., Chisholm, J., Furlanetto, S. R., & Mason, C. 2024, MNRAS, 535, L37  
 Naidu, R. P., Tacchella, S., Mason, C. A., et al. 2020, ApJ, 892, 109  
 Nakajima, K., Ouchi, M., Isobe, Y., et al. 2024, arXiv e-prints, arXiv:2412.04541  
 Nakajima, K., Ouchi, M., Xu, Y., et al. 2022, ApJS, 262, 3  
 Price, S. H., Bezanson, R., Labbe, I., et al. 2025, ApJ, 982, 51  
 Robertson, B. E. 2022, ARA&A, 60, 121  
 Sanders, R. L., Shapley, A. E., Topping, M. W., et al. 2025, eprint arXiv:2508.10099  
 Schaefer, D. 2003, A&A, 397, 527  
 Scholtz, J., Carniani, S., Parlanti, E., et al. 2025, eprint arXiv:2510.01034, arXiv:2510.01034  
 Simmonds, C., Tacchella, S., Hainline, K., et al. 2024, MNRAS, 535, 2998  
 Singh, A., Malhotra, S., & Ely Rhoads, J. 2025, eprint arXiv:2510.26990, arXiv:2510.26990  
 Storey, P. J. & Zeippen, C. J. 2000, MNRAS, 312, 813  
 Suess, K. A., Weaver, J. R., Price, S. H., et al. 2024, ApJ, 976, 101  
 Vanzella, E., Loiacono, F., Bergamini, P., et al. 2023, A&A, 678, A173  
 Vanzella, E., Loiacono, F., Messa, M., et al. 2024, A&A, 691, A251  
 Vanzella, E., Messa, M., Zanella, A., et al. 2025, arXiv e-prints, arXiv:2509.07073  
 Virtanen, P., Gommers, R., Oliphant, T. E., et al. 2020, Nature Medicine, 17, 261  
 Willott, C. J., Asada, Y., Iyer, K. G., et al. 2025, ApJ, 988, 26

## Appendix A: Fitting emission lines

To measure the line flux of the [O III] and H $\beta$  lines, we first fitted the continuum. For that, we selected small regions around the lines and masked them. We also manually checked each spectrum and removed contaminating features from other objects. Then, we fitted a 1st order polynomial to the continuum, which was then subtracted from the spectrum. To model the emission lines, we use one Gaussian profile per line. For [O III]+H $\beta$ , this yield nine free parameters, which can be reduced with three physical considerations: The rest-frame wavelengths are fixed by physics and can be reduced to one physical parameter governed by the redshift. Then, the amplitude between the two [O III] doublet is fixed to 2.98 (Storey & Zeippen 2000), reducing them to one free parameter. Finally, we expect the [O III] doublet to come from the same region, and therefore have the same velocity profile, so the standard deviation is common to the two Gaussians. We end up with five free parameters ( $z$ ,  $A_{H\beta}$ ,  $A_{[O\text{ III}]\lambda 5008}$ ,  $\sigma_{H\beta}$  and  $\sigma_{[O\text{ III}]\lambda 5008}$ , where  $A$  are the Gaussian amplitudes and  $\sigma$  are standard deviations), that we optimise with a Monte-Carlo Markov-Chain (MCMC). Note that the spectra of two galaxies show broader components. We fitted only the narrow component, leaving the detailed analysis for other GLIMPSE papers (see Berg et al. (2025) and Korber et al. (in prep)). Fig. A.1 shows four galaxies with their associated fits. The measured line flux are found in Table C.1.

## Appendix B: Measuring $\dot{N}_{\text{ion}}$ from the [O III]+H $\beta$ LF

The ionising photon production rate  $\dot{N}_{\text{ion}}$  can be directly obtained from the H $\alpha$  LF (or H $\beta$  LF, accounting for dust attenuation and a fixed H $\alpha$ -to-H $\beta$  ratio)  $\phi$  following:

$$\dot{N}_{\text{ion}} = \int_{L_{\text{min}}}^{\infty} f_{\text{esc}} Q_{\text{ion}}(L) \phi(L) dL \quad (\text{B.1})$$

$$= \int_{L_{\text{min}}}^{\infty} f_{\text{esc}} \frac{L}{c_{\alpha}(1 - f_{\text{esc}})} \phi(L) dL \quad (\text{B.2})$$

For this, we assumed a constant  $f_{\text{esc}} = 14\%$ , following the measurements of Jecmen et al. (Submitted) for the GLIMPSE photometric sample. Their measurements span galaxies down to  $M_{\text{UV}} \gtrsim -12.5$  using the UV continuum slopes. We also adopted the ratio between the line emissivity and the total recombination rate  $c_{\alpha} = 1.37 \times 10^{-12}$  erg for an electron temperature of  $10^4$  K (Schaerer 2003). The ionising photon production rate  $Q_{\text{ion}}(L)$  is related to luminosity with  $L = Q_{\text{ion}} c_{\alpha} (1 - f_{\text{esc}})$ . The relative contribution of each luminosity bin in Fig. 4 is measured by calculating the difference between all the  $\dot{N}_{\text{ion}}$  data point and normalising it by the  $\dot{N}_{\text{ion}}$  at  $L_{\text{H}\alpha} = 10^{36} \text{ s}^{-1} \text{Mpc}^{-3}$ .

## Appendix C: Table of emission lines

We report in C.1 the measurements of the galaxies considered in this letter.

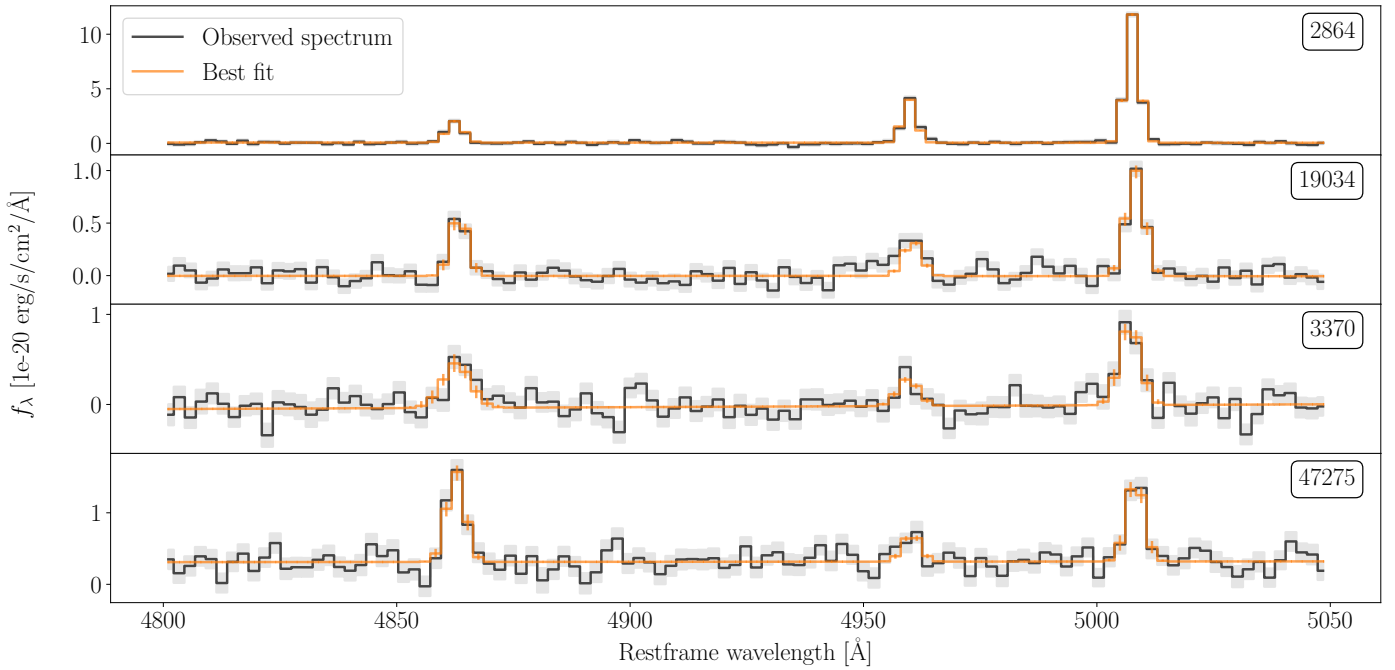


Fig. A.1: Four galaxies with their observed spectrum and their associated best fit model. The galaxies are ordered by their R3 (from highest to lowest).

ID	RA deg	DEC deg	$z_{\text{spec}}$	$M_{\text{UV}}$ AB mag	$\mu$	[O III] $\lambda 5008$ 10 $^{-19}$ egs	H $\beta$ 10 $^{-19}$ egs	R3	12+log(O/H)
(1)	(2)	(3)	(4)	(5)	(6)	(7)	(8)	(9)	(10)
2401	342.22476	-44.56736	7.9235	-20.11	$1.37 \pm 0.02$	$34.28^{+0.77}_{-0.97}$	$6.29^{+0.47}_{-0.60}$	$5.35^{+0.44}_{-0.49}$	$7.72^{+0.24}_{-0.24}$
2864	342.23004	-44.56598	6.4890	-17.93	$1.28 \pm 0.01$	$26.21^{+0.40}_{-0.40}$	$5.17^{+0.30}_{-0.30}$	$5.07^{+0.32}_{-0.29}$	$7.68^{+0.24}_{-0.23}$
3370	342.22861	-44.56467	6.1738	-17.19	$1.29 \pm 0.02$	$2.91^{+0.35}_{-0.33}$	$2.14^{+0.43}_{-0.38}$	$1.36^{+0.34}_{-0.27}$	$7.05^{+0.25}_{-0.25}$
4164	342.21524	-44.56320	6.1757	-18.53	$1.39 \pm 0.03$	$5.82^{+0.30}_{-0.34}$	$1.18^{+0.46}_{-0.34}$	$4.84^{+1.80}_{-1.42}$	$7.65^{+0.37}_{-0.30}$
5381	342.26215	-44.56067	7.5492	-19.15	$1.22 \pm 0.01$	$61.29^{+0.73}_{-0.78}$	$9.93^{+0.57}_{-0.48}$	$6.17^{+0.33}_{-0.35}$	$7.94^{+0.23}_{-0.26}$
5536	342.25626	-44.56019	6.2228	nan	$1.23 \pm 0.01$	$5.02^{+0.22}_{-0.22}$	$1.11^{+0.20}_{-0.20}$	$4.46^{+0.95}_{-0.73}$	$7.60^{+0.27}_{-0.25}$
6170	342.25748	-44.55910	6.4367	-18.62	$1.23 \pm 0.01$	$31.23^{+0.38}_{-0.37}$	$4.30^{+0.18}_{-0.17}$	$7.26^{+0.32}_{-0.30}$	$7.95^{+0.23}_{-0.23}$
6297	342.21240	-44.55897	7.1221	nan	$1.44 \pm 0.03$	$42.49^{+1.54}_{-1.55}$	$12.98^{+1.52}_{-1.48}$	$3.28^{+0.44}_{-0.36}$	$7.44^{+0.24}_{-0.24}$
6358	342.26428	-44.55873	6.2252	-18.96	$1.22 \pm 0.01$	$9.62^{+0.31}_{-0.32}$	$4.07^{+0.31}_{-0.32}$	$2.36^{+0.21}_{-0.18}$	$7.29^{+0.23}_{-0.23}$
6408	342.26740	-44.55862	6.4388	-17.53	$1.21 \pm 0.01$	$11.09^{+0.28}_{-0.37}$	$1.76^{+0.36}_{-0.30}$	$6.20^{+1.21}_{-1.21}$	$7.94^{+0.23}_{-0.35}$
6587	342.26785	-44.55857	6.4380	-19.39	$1.21 \pm 0.01$	$30.61^{+0.56}_{-0.56}$	$4.78^{+0.51}_{-0.50}$	$6.39^{+0.76}_{-0.64}$	$7.94^{+0.23}_{-0.27}$
7468	342.25397	-44.55680	6.1124	-19.23	$1.25 \pm 0.02$	$45.28^{+0.68}_{-0.67}$	$6.71^{+0.32}_{-0.31}$	$6.74^{+0.35}_{-0.32}$	$7.94^{+0.23}_{-0.23}$
7685	342.24686	-44.55608	6.4175	-16.59	$1.28 \pm 0.02$	$3.41^{+0.25}_{-0.26}$	$1.05^{+0.29}_{-0.25}$	$3.24^{+0.96}_{-0.71}$	$7.43^{+0.27}_{-0.26}$
8139	342.26129	-44.55530	6.2238	-16.45	$1.24 \pm 0.01$	$7.48^{+0.29}_{-0.29}$	$1.37^{+0.24}_{-0.24}$	$5.46^{+1.19}_{-0.88}$	$7.74^{+0.30}_{-0.26}$
8172	342.24261	-44.55537	6.2199	-17.49	$1.29 \pm 0.02$	$31.88^{+0.78}_{-0.81}$	$3.97^{+0.79}_{-0.66}$	$7.82^{+1.24}_{-1.24}$	$7.95^{+0.23}_{-0.23}$
8192	342.24255	-44.55531	6.2199	-18.27	$1.29 \pm 0.02$	$16.62^{+0.52}_{-0.56}$	$3.98^{+1.18}_{-0.91}$	$4.12^{+1.28}_{-0.99}$	$7.55^{+0.29}_{-0.27}$
8947	342.26410	-44.55429	6.2208	-18.77	$1.23 \pm 0.01$	$17.10^{+0.54}_{-0.59}$	$2.62^{+0.48}_{-0.41}$	$6.50^{+1.19}_{-1.03}$	$7.94^{+0.23}_{-0.30}$
8981	342.18991	-44.55407	6.5588	-19.09	$1.61 \pm 0.03$	$37.45^{+0.80}_{-0.79}$	$6.67^{+0.49}_{-0.47}$	$5.62^{+0.44}_{-0.39}$	$7.77^{+0.26}_{-0.24}$
9081	342.25659	-44.55378	6.2222	-16.97	$1.26 \pm 0.01$	$6.90^{+0.29}_{-0.29}$	$1.14^{+0.29}_{-0.25}$	$6.01^{+1.58}_{-1.20}$	$7.87^{+0.24}_{-0.32}$
9214	342.25241	-44.55355	6.5491	-17.22	$1.27 \pm 0.02$	$8.62^{+0.21}_{-0.23}$	$2.43^{+0.23}_{-0.23}$	$3.52^{+0.36}_{-0.33}$	$7.47^{+0.24}_{-0.23}$
9751	342.19452	-44.55263	6.5110	-16.39	$1.77 \pm 0.05$	$2.40^{+0.23}_{-0.22}$	$0.40^{+0.27}_{-0.23}$	$4.96^{+2.61}_{-1.70}$	$7.67^{+0.37}_{-0.33}$
10182	342.24286	-44.55198	6.5175	-17.90	$1.31 \pm 0.02$	$5.10^{+0.33}_{-0.35}$	$2.49^{+0.39}_{-0.37}$	$2.04^{+0.38}_{-0.32}$	$7.23^{+0.24}_{-0.24}$
10357	342.24915	-44.55183	6.0600	-18.91	$1.29 \pm 0.02$	$84.80^{+1.14}_{-1.14}$	$13.86^{+0.51}_{-0.49}$	$6.12^{+0.24}_{-0.23}$	$7.94^{+0.23}_{-0.25}$
11482	342.26190	-44.54998	6.5060	-16.74	$1.26 \pm 0.01$	$5.35^{+0.34}_{-0.31}$	$1.29^{+0.51}_{-0.39}$	$4.11^{+1.72}_{-1.19}$	$7.55^{+0.35}_{-0.29}$
11525	342.24811	-44.54990	6.5049	-18.33	$1.31 \pm 0.02$	$5.49^{+0.27}_{-0.28}$	$2.63^{+0.29}_{-0.29}$	$2.09^{+0.27}_{-0.23}$	$7.24^{+0.24}_{-0.24}$
11789	342.25421	-44.54950	6.5211	-16.69	$1.28 \pm 0.02$	$7.65^{+0.44}_{-0.47}$	$2.61^{+0.48}_{-0.49}$	$2.91^{+0.63}_{-0.48}$	$7.38^{+0.25}_{-0.24}$
12248	342.23199	-44.54891	6.1081	-17.87	$1.40 \pm 0.02$	$34.89^{+0.71}_{-0.80}$	$7.16^{+0.32}_{-0.28}$	$4.87^{+0.22}_{-0.25}$	$7.65^{+0.23}_{-0.23}$
12801	342.24939	-44.54817	7.5686	-18.76	$1.31 \pm 0.02$	$28.49^{+0.52}_{-0.51}$	$5.08^{+0.36}_{-0.35}$	$5.61^{+0.42}_{-0.38}$	$7.77^{+0.25}_{-0.24}$
13186	342.17361	-44.54759	6.1571	-16.35	$2.90 \pm 0.09$	$1.04^{+0.15}_{-0.14}$	$0.83^{+0.20}_{-0.17}$	$1.25^{+0.36}_{-0.29}$	$7.01^{+0.26}_{-0.26}$
13882	342.23651	-44.54689	6.1074	-19.17	$1.39 \pm 0.02$	$46.52^{+1.03}_{-1.15}$	$7.81^{+0.61}_{-0.67}$	$5.90^{+0.51}_{-0.50}$	$7.83^{+0.25}_{-0.25}$
13941	342.23645	-44.54690	6.1075	-19.18	$1.39 \pm 0.03$	$18.63^{+0.44}_{-0.44}$	$2.63^{+0.25}_{-0.23}$	$7.09^{+0.71}_{-0.63}$	$7.95^{+0.23}_{-0.23}$
14311	342.17770	-44.54694	6.0027	-17.97	$3.54 \pm 0.12$	$6.13^{+0.33}_{-0.37}$	$0.94^{+0.25}_{-0.25}$	$6.18^{+1.65}_{-1.46}$	$7.94^{+0.23}_{-0.38}$
14499	342.25143	-44.54671	6.1063	-20.16	$1.31 \pm 0.02$	$106.60^{+1.49}_{-1.47}$	$14.16^{+0.58}_{-0.56}$	$7.53^{+0.33}_{-0.31}$	$7.95^{+0.23}_{-0.23}$
17070	342.17825	-44.54387	6.0296	-15.32	$5.80 \pm 0.28$	$0.61^{+0.06}_{-0.06}$	$0.28^{+0.06}_{-0.05}$	$2.22^{+0.55}_{-0.41}$	$7.26^{+0.25}_{-0.25}$
19034	342.21237	-44.52876	6.2025	-15.88	$2.93 \pm 0.15$	$1.25^{+0.10}_{-0.11}$	$0.67^{+0.09}_{-0.09}$	$1.83^{+0.30}_{-0.26}$	$7.18^{+0.24}_{-0.24}$
26653	342.18408	-44.53164	6.1044	-19.81	$1.96 \pm 0.36$	$130.85^{+28.92}_{-20.15}$	$20.76^{+4.59}_{-3.19}$	$6.21^{+1.66}_{-1.39}$	$7.94^{+0.23}_{-0.37}$
37914	342.18845	-44.53619	6.1096	-15.36	$16.29 \pm 1.62$	$1.03^{+0.12}_{-0.10}$	$0.35^{+0.06}_{-0.06}$	$2.99^{+0.67}_{-0.54}$	$7.39^{+0.25}_{-0.25}$
38657	342.24072	-44.53654	6.2117	-17.78	$1.47 \pm 0.03$	$5.26^{+0.44}_{-0.45}$	$1.24^{+0.64}_{-0.51}$	$3.97^{+2.24}_{-1.37}$	$7.53^{+0.47}_{-0.31}$
38807	342.23361	-44.53667	7.7668	-18.02	$1.59 \pm 0.03$	$8.40^{+0.51}_{-0.52}$	$1.71^{+0.79}_{-0.68}$	$4.64^{+2.34}_{-1.56}$	$7.62^{+0.40}_{-0.31}$
41948	342.19086	-44.53749	6.1044	nan	$6.22 \pm 0.42$	$145.79^{+10.54}_{-9.40}$	$22.47^{+1.65}_{-1.44}$	$6.49^{+0.66}_{-0.61}$	$7.94^{+0.23}_{-0.26}$
42531	342.22708	-44.53763	6.2075	-17.91	$1.67 \pm 0.04$	$29.08^{+2.67}_{-24.30}$	$0.36^{+0.50}_{-0.25}$	$2.68^{+3.60}_{-1.76}$	$7.34^{+0.64}_{-0.54}$
42812	342.24670	-44.53885	6.5932	-18.68	$1.39 \pm 0.03$	$8.09^{+0.49}_{-0.48}$	$1.74^{+0.63}_{-0.55}$	$4.57^{+1.94}_{-1.20}$	$7.61^{+0.40}_{-0.28}$
43280	342.24637	-44.53909	6.2242	-17.50	$1.39 \pm 0.02$	$4.48^{+0.32}_{-0.35}$	$1.09^{+0.41}_{-0.33}$	$4.03^{+1.67}_{-1.13}$	$7.54^{+0.34}_{-0.28}$
43555	342.26297	-44.53924	6.2064	-17.09	$1.30 \pm 0.02$	$6.86^{+0.34}_{-0.38}$	$1.25^{+0.37}_{-0.30}$	$5.44^{+1.61}_{-1.35}$	$7.74^{+0.31}_{-0.30}$
45084	342.25854	-44.54039	6.4940	-16.58	$1.31 \pm 0.02$	$3.34^{+0.24}_{-0.24}$	$1.45^{+0.25}_{-0.25}$	$2.31^{+0.48}_{-0.37}$	$7.28^{+0.24}_{-0.24}$
45706	342.23682	-44.54075	6.4150	-16.05	$1.46 \pm 0.03$	$3.75^{+0.34}_{-0.44}$	$2.03^{+0.33}_{-0.40}$	$1.83^{+0.39}_{-0.30}$	$7.18^{+0.24}_{-0.24}$

ID	RA deg	DEC deg	$z_{\text{spec}}$	$M_{\text{UV}}$ AB mag	$\mu$	[O III] $\lambda 5008$ $10^{-19}$ egs	H $\beta$ $10^{-19}$ egs	R3	12+log(O/H)
(1)	(2)	(3)	(4)	(5)	(6)	(7)	(8)	(9)	(10)
45883	342.24643	-44.54088	6.2220	-17.95	$1.38 \pm 0.02$	$22.14^{+0.40}_{-0.42}$	$4.19^{+0.19}_{-0.17}$	$5.29^{+0.24}_{-0.25}$	$7.71^{+0.23}_{-0.23}$
46408	342.18414	-44.54120	6.5361	-15.93	$6.29 \pm 0.39$	$0.84^{+0.07}_{-0.06}$	$0.12^{+0.04}_{-0.04}$	$6.45^{+1.86}_{-1.45}$	$7.94^{+0.23}_{-0.35}$
46431	342.23651	-44.54118	6.5221	-15.88	$1.45 \pm 0.02$	$2.35^{+0.25}_{-0.26}$	$0.95^{+0.38}_{-0.31}$	$2.39^{+1.18}_{-0.77}$	$7.29^{+0.29}_{-0.28}$
46938	342.23605	-44.54156	6.8526	-18.52	$1.46 \pm 0.03$	$36.01^{+0.79}_{-0.85}$	$6.87^{+0.28}_{-0.31}$	$5.23^{+0.25}_{-0.24}$	$7.71^{+0.23}_{-0.23}$
47275	342.24191	-44.54156	6.4427	-16.84	$1.40 \pm 0.02$	$2.99^{+0.32}_{-0.33}$	$3.36^{+0.33}_{-0.34}$	$0.89^{+0.14}_{-0.12}$	$6.84^{+0.24}_{-0.25}$
47757	342.17593	-44.54240	6.0014	-14.63	$14.67 \pm 1.40$	$0.80^{+0.09}_{-0.07}$	$0.32^{+0.04}_{-0.03}$	$2.52^{+0.41}_{-0.37}$	$7.32^{+0.24}_{-0.24}$
54637	342.20590	-44.51908	6.0647	-15.39	$16.12 \pm 8.09$	$9.46^{+13.26}_{-6.87}$	$10.23^{+14.16}_{-7.24}$	$2.26^{+2.85}_{-1.35}$	$7.27^{+0.48}_{-0.48}$
56616	342.22980	-44.54204	8.6354	-17.85	$1.52 \pm 0.04$	$0.23^{+0.21}_{-0.08}$	$0.09^{+0.11}_{-0.06}$	$2.27^{+0.71}_{-0.47}$	$7.27^{+0.26}_{-0.25}$

Table C.1: Catalogue and properties of the sources (1) GLIMPSE identification number (2 & 3) Right Ascension and DEClination in J2000 (4) spectroscopic redshift from emission line fit (5) intrinsic UV magnitude. Note that sources with missing  $M_{\text{UV}}$  have a poor photometric constraints. (6) Lensing magnification (7 & 8) intrinsic line flux of [O III] $\lambda 5008$  and H $\beta$  (egs = erg/s/cm $^2$ ) (9) R3 = [O III] $\lambda 5008$ /H $\beta$  (10) Oxygen abundance from (Nakajima et al. 2022). Line fluxes and  $M_{\text{UV}}$  were corrected for lensing magnification. To retrieve the observed quantities, multiple line flux by  $\mu$  and subtract  $2.5 \log_{10}(\mu)$  to  $M_{\text{UV}}$ .